# Computational Homogenization for Inverse Design of Surface-based Inflatables
## Supplementary Document

Yingying Ren, Julian Panetta, Seiichi Suzuki, Uday Kusupati, Florin Isvoranu, Mark Pauly

This document provides physical validation experiments and more details on the derivations of various formulas and methods stated in the main paper [Ren et al., 2024].
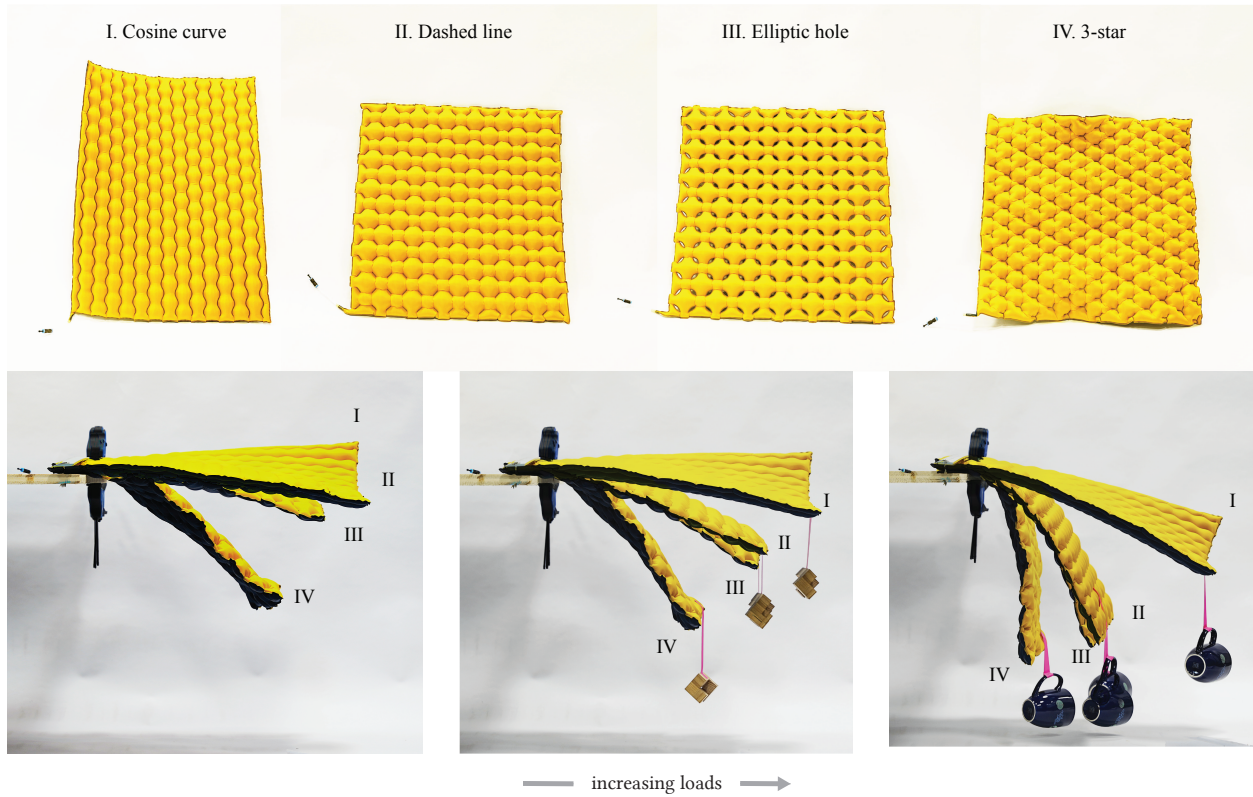
## 1    Physical Validations



**Figure 1** *Physical validation of pattern homogenization. We fabricated tessellations of the representative unit cells shown in the main paper, inflated them to the same pressure, and conducted load tests. The tessellations exhibit the expected behavior of the homogenized material properties. In particular, the 3-star pattern has weak bending stiffnesses despite having similar geometric features to the dashed line pattern.*
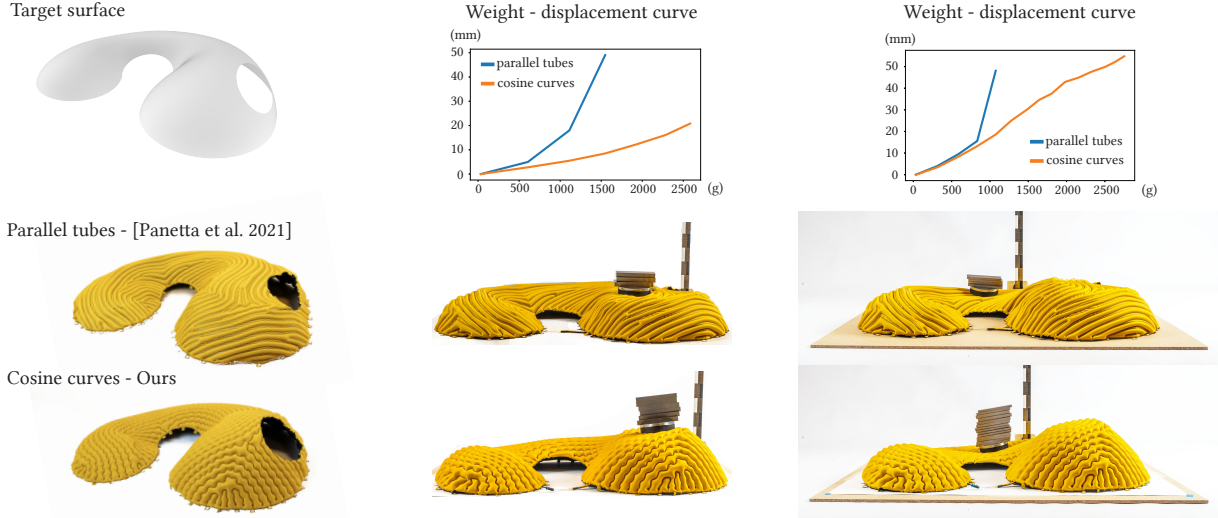
Target surface

Weight - displacement curve

Weight - displacement curve

Parallel tubes - [Panetta et al. 2021]

Cosine curves - Ours

**Figure 2** *Comparisons between simulation and physical prototypes for the parallel tubes of [Panetta et al., 2021] and our approach. The second and third columns show two basic load-testing experiments. See also accompanying video for an animation of the experiments.*

# 2 Bending the Midsurface

The following subsections investigate details related to the macroscopic bending deformation illustrated in Figure 3.



Macro Membrane Strain $\overline{S}$

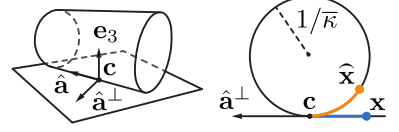Macro Bending $(\overline{\kappa}, \hat{\mathbf{a}})$

**Figure 3** *Deformations applied to an infinite periodic sheet tiling during homogenization (left): first an in-plane constant macroscopic stretch is applied and the sheet relaxes into a (potentially non-planar) periodic fluctuation displacement around the linear deformation (middle). Second, the entire tiling is bent into a surface of constant curvature (right).*

## 2.1 Single Axis Bending

We pick a "center" point $\mathbf{c}$ on the $x_3 = 0$ plane of the unbent unit cell to remain fixed under this wrapping and note that traversing the geodesic of the cylinder corresponding to tangent vector $\mathbf{v}$ at $\mathbf{c}$ induces a rotation of the tangent plane by $\overline{\kappa}(\hat{\mathbf{a}}^\perp \cdot \mathbf{v})$ around $\hat{\mathbf{a}}$. Therefore, the orientation of the tangent plane at any point $\hat{\mathbf{x}}$ of the bent tiling relative to the (unbent) tangent plane at $\mathbf{c}$ can be represented by the angle-scaled-axis

vector $\boldsymbol{\omega} = \overline{\kappa}\hat{\mathbf{a}}(\hat{\mathbf{a}}^{\perp} \cdot \mathbf{v}) = \nabla\boldsymbol{\omega}(\mathbf{x} - \mathbf{c})$ where $\nabla\boldsymbol{\omega} = \overline{\kappa}\hat{\mathbf{a}} \otimes \hat{\mathbf{a}}^{\perp}$. The corresponding rotation matrix is given by $e^{[\boldsymbol{\omega}]_{\times}} = I + \sin(\|\boldsymbol{\omega}\|)\,[\hat{\boldsymbol{\omega}}]_{\times} + (1 - \cos(\|\boldsymbol{\omega}\|))\,[\hat{\boldsymbol{\omega}}]_{\times}^{2}$. Furthermore, we can calculate the bent coordinates $\hat{\mathbf{x}}$ of a point $\mathbf{x}$ also on the $x_3 = 0$ plane in the unbent tiling by integrating along the geodesic connecting it to $\mathbf{c}$:

$$
\begin{aligned}
\hat{\mathbf{x}} &= \mathbf{c} + \int_0^1 e^{t[\nabla\boldsymbol{\omega}(\mathbf{x}-\mathbf{c})]_{\times}}(\mathbf{x} - \mathbf{c})\,\mathrm{d}t \\
&= \mathbf{c} + \left[I + \left(\frac{1 - \cos(\|\boldsymbol{\omega}\|)}{\|\boldsymbol{\omega}\|^2}\right)[\boldsymbol{\omega}]_{\times} + \left(\frac{\|\boldsymbol{\omega}\| - \sin(\|\boldsymbol{\omega}\|)}{\|\boldsymbol{\omega}\|^3}\right)[\boldsymbol{\omega}]_{\times}^2\right](\mathbf{x} - \mathbf{c}) \\
&= \mathbf{x} + \left[\left(\frac{1 - \cos(\|\boldsymbol{\omega}\|)}{\|\boldsymbol{\omega}\|^2}\right)[\boldsymbol{\omega}]_{\times} + \left(\frac{\|\boldsymbol{\omega}\| - \sin(\|\boldsymbol{\omega}\|)}{\|\boldsymbol{\omega}\|^3}\right)[\boldsymbol{\omega}]_{\times}^2\right](\mathbf{x} - \mathbf{c}).
\end{aligned}
$$

$$\text{(A1)}$$

## 2.2 Dependence on Choice of c

The requirement to pick a fixed point $\mathbf{c}$ for the wrapping raises concerns that the homogenized properties change with different selections. However, here we show that *under single-axis bending*, different selections produce wrappings differing only by a rigid transformation (and thus identical homogenized properties).

We first rearrange the $\hat{\mathbf{x}}$ formula above into a more geometrically meaningful form, making use of the relationships:

$$
\hat{\mathbf{a}}^{\perp} \cdot (\mathbf{x} - \mathbf{c}) = \frac{\|\boldsymbol{\omega}\|}{\overline{\kappa}},
$$

$$
\boldsymbol{\omega} \times (\mathbf{x} - \mathbf{c}) = \|\boldsymbol{\omega}\|\hat{\mathbf{a}} \times (\mathbf{x} - \mathbf{c}) = \mathbf{e}_3\|\boldsymbol{\omega}\|\hat{\mathbf{a}}^{\perp} \cdot (\mathbf{x} - \mathbf{c}) = \mathbf{e}_3\frac{\|\boldsymbol{\omega}\|^2}{\overline{\kappa}},
$$

$$
[\boldsymbol{\omega}]_{\times}^2 (\mathbf{x} - \mathbf{c}) = \boldsymbol{\omega} \times \left(\mathbf{e}_3\frac{\|\boldsymbol{\omega}\|^2}{\overline{\kappa}}\right) = \frac{\|\boldsymbol{\omega}\|^3}{\overline{\kappa}}\hat{\mathbf{a}} \times \mathbf{e}_3 = -\frac{\|\boldsymbol{\omega}\|^3}{\overline{\kappa}}\hat{\mathbf{a}}^{\perp}.
$$

Therefore:

$$
\begin{aligned}
\hat{\mathbf{x}} &= \mathbf{x} + \left(\frac{1 - \cos(\|\boldsymbol{\omega}\|)}{\overline{\kappa}}\right)\mathbf{e}_3 - \left(\frac{\|\boldsymbol{\omega}\| - \sin(\|\boldsymbol{\omega}\|)}{\overline{\kappa}}\right)\hat{\mathbf{a}}^{\perp} \\
&= \mathbf{x} - (\hat{\mathbf{a}}^{\perp} \otimes \hat{\mathbf{a}}^{\perp})(\mathbf{x} - \mathbf{c}) + \frac{1}{\overline{\kappa}}\left[\mathbf{e}_3 + \sin(\|\boldsymbol{\omega}\|)\hat{\mathbf{a}}^{\perp} - \cos(\|\boldsymbol{\omega}\|)\mathbf{e}_3\right] \\
&= \mathbf{c} + (I - \hat{\mathbf{a}}^{\perp} \otimes \hat{\mathbf{a}}^{\perp})(\mathbf{x} - \mathbf{c}) + \frac{1}{\overline{\kappa}}\left[\mathbf{e}_3 + \sin(\|\boldsymbol{\omega}\|)\hat{\mathbf{a}}^{\perp} - \cos(\|\boldsymbol{\omega}\|)\mathbf{e}_3\right] \\
&= \left(\mathbf{c} + \frac{1}{\overline{\kappa}}\mathbf{e}_3\right) + \hat{\mathbf{a}} \otimes \hat{\mathbf{a}}(\mathbf{x} - \mathbf{c}) - \frac{1}{\overline{\kappa}}e^{[\nabla\boldsymbol{\omega}(\mathbf{x}-\mathbf{c})]_{\times}}\mathbf{e}_3.
\end{aligned}
$$

This formula makes it geometrically obvious that the $x_3 = 0$ plane is indeed wrapped onto a radius $\frac{1}{\overline{\kappa}}$ cylinder with axis passing through point $\mathbf{c} + \frac{1}{\overline{\kappa}}\mathbf{e}_3$ along direction $\hat{\mathbf{a}}$. Now, manipulating slightly further:

$$
\begin{aligned}
\hat{\mathbf{x}} &= (\hat{\mathbf{a}} \otimes \hat{\mathbf{a}})\mathbf{x} - \frac{1}{\overline{\kappa}}e^{[\nabla\boldsymbol{\omega}(\mathbf{x}-\mathbf{c})]_{\times}}\mathbf{e}_3 + \mathbf{t}_c \\
&= e^{[-\nabla\mathbf{c}]_{\times}}\left((\hat{\mathbf{a}} \otimes \hat{\mathbf{a}})\mathbf{x} - \frac{1}{\overline{\kappa}}e^{[\nabla\boldsymbol{\omega}\mathbf{x}]_{\times}}\mathbf{e}_3\right) + \mathbf{t}_c,
\end{aligned}
$$

where $\mathbf{t}_c = \left(\mathbf{c} + \frac{1}{\overline{\kappa}}\mathbf{e}_3\right) - (\hat{\mathbf{a}} \otimes \hat{\mathbf{a}})\mathbf{c}$. Here, we used the fact that rotations $e^{[\nabla\boldsymbol{\omega}\mathbf{c}]_{\times}}$ and $e^{[\nabla\boldsymbol{\omega}\mathbf{x}]_{\times}}$ are both *around the same axis* $\hat{\mathbf{a}}$ (which does not hold in the general case of multi-axis bending!) to factor out the $\mathbf{c}$-dependent part of the rotation. This shows $\hat{\mathbf{x}}$ to be a rigid transformation of the $\mathbf{c}$-independent cylinder $(\hat{\mathbf{a}} \otimes \hat{\mathbf{a}})\mathbf{x} - \frac{1}{\overline{\kappa}}e^{[\nabla\boldsymbol{\omega}\mathbf{x}]_{\times}}\mathbf{e}_3$. In other words, all choices of $\mathbf{c}$ produce rigid transformations of the same cylinder, as we wished to prove.

## 2.3  Double Curvature

The formula for $\widehat{\mathbf{x}}$ generalizes to the double-curvature setting by taking $\boldsymbol{\omega} = \nabla \boldsymbol{\omega} \mathbf{x}$ with $\nabla \boldsymbol{\omega} = \overline{\kappa}_1 \hat{\mathbf{a}} \otimes \hat{\mathbf{a}}^\perp + \overline{\kappa}_2 \hat{\mathbf{a}}^\perp \otimes \hat{\mathbf{a}}$. However, the resulting deformation is dependent on the choice of $\mathbf{c}$, and the deformed unit cells no longer tile seamlessly:
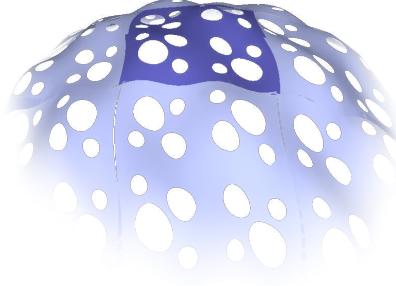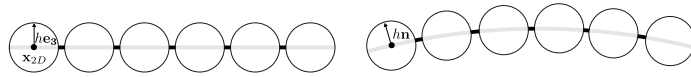


**Figure 4** *An attempt to apply the bent tiling formulas to a state of double curvature (here, picking $\mathbf{c}$ at the center of the blue tile); notice the gaps appearing between unit cells.*

# 3  Single-axis Bending of Thickened Unit Cell



Formula (A1) for $\widehat{\mathbf{x}}$ is a bending motion only for points on the macroscopic midsurface ($x_3 = \mathbf{e}_3 \cdot \mathbf{x} = 0$). We extend this bending deformation the full space using the formula:

$$\widehat{\mathbf{x}}(\mathbf{x}) = \mathbf{x}_{2D} + \left[ \left( \frac{1 - \cos(\|\boldsymbol{\omega}\|)}{\|\boldsymbol{\omega}\|^2} \right) [\boldsymbol{\omega}]_\times + \left( \frac{\|\boldsymbol{\omega}\| - \sin(\|\boldsymbol{\omega}\|)}{\|\boldsymbol{\omega}\|^3} \right) [\boldsymbol{\omega}]_\times^2 \right] (\mathbf{x}_{2D} - \mathbf{c}) + u_3 e^{[\boldsymbol{\omega}]_\times} \mathbf{e}_3, \qquad \text{(A2)}$$

where $\mathbf{x}_{2D} = (I - \mathbf{e}_3 \otimes \mathbf{e}_3)\mathbf{x}$ and $u_3 = \mathbf{e}_3 \cdot \mathbf{x}$. In other words, points at normal offset $u_3$ from the flat initial midsurface remain at offset $u_3$ along the rotated normal $e^{[\boldsymbol{\omega}]_\times} \mathbf{e}_3$ from the bent midsurface.

## 3.1  Stretch-Bend Ambiguity under Normal Offset

We note that the Kirchhoff-Love-type bending deformation (A2) stretches material "above" and compresses material "below" the $x_3 = 0$ midsurface. Thus, although the periodic deformation described by a particular macroscopic state $(\overline{S}, \overline{\kappa}, \overline{\alpha})$ is invariant to in-plane translations $\mathbf{u} \to \mathbf{u} + \alpha \mathbf{e}_1 + \beta \mathbf{e}_2$, it is affected by normal translations $\mathbf{u} \to \mathbf{u} + h\mathbf{e}_3$. In other words, it is sensitive to the vertical positioning of the microscopic geometry within the unit cell. A natural way to resolve this is to constrain $\overline{h} := \int_\Gamma \mathbf{u} \cdot \mathbf{e}_3 \, \mathrm{d}A(\mathbf{x}) = 0$, defining the macroscopic midsurface to pass through the "center" of the microscopic geometry; this is similar in spirit to the more complicated "parallel-transported" constraint imposed in [Sperl et al., 2020]. However, even with this simplified formulation, care must be taken to implement this global constraint in a way that does not excessively sacrifice sparsity; [Sperl et al., 2020] resort to enforcing it via Lagrange multipliers, which involves solving a more expensive, indefinite KKT system at each Newton step (and losing the ability to detect indefiniteness "for free" from the Cholesky factorization).

We propose instead to resolve the ambiguity by establishing an equivalence between macroscopic states $(\overline{S}_{\overline{h}}, \overline{\kappa}_{\overline{h}}, \overline{\alpha}, \overline{h})$ with different offsets $\overline{h}$ of the "true" macroscopic midsurface from the $x_3 = 0$ midplane. Our approach is especially convenient for inflatables homogenization, where we need not *impose* $\overline{S}_0$ or $(\overline{\kappa}_0, \overline{\alpha}_0)$ directly but rather wish to study the macroscopic deformation that arises under pressure actuation. If

a precise stretching and bending state must be imposed at $\bar{h} = 0$, this still can be done with an outer optimization over either the imposed $(\overline{S}_{\bar{h}}, \overline{\kappa}_{\bar{h}}, \overline{\alpha}_{\bar{h}})$ or the parameter controlling $\bar{h}$ (*e.g.*, the right-hand-side of a pin constraint).

Specifically, we note that the vertical offset $\bar{h}$ adds to the radius of curvature, meaning the curvature of the "true" midsurface at $x_3 = \bar{h}$ is $\overline{\kappa}_0 = \frac{1}{\bar{h} + 1/\overline{\kappa}_{\bar{h}}}$. Furthermore, bending by $\overline{\kappa}_{\bar{h}} \overline{\alpha}_{\bar{h}}$ stretches the plane $x_3 = \bar{h}$ along the $\hat{\mathbf{a}}^\perp$ axis by a factor of $\bar{h}\overline{\kappa}_{\bar{h}}$, establishing a true midsurface stretch of $\overline{S}_0 = (I + \bar{h}\overline{\kappa}_{\bar{h}} \hat{\mathbf{a}}^\perp \otimes \hat{\mathbf{a}}^\perp)\overline{S}_{\bar{h}}$. (Note, $\overline{S}_0$ is no longer symmetric in general, but its symmetric part can be extracted via a polar decomposition, and then $\overline{\alpha}$ can be adjusted to account for the effective rotation this applied to the stretched tiling). Hence, after performing a simulation using any means to constrain vertical motion (*e.g.*, a pin constraint or a small Hessian shift), one obtains the deformed macro + micro state $(\overline{S}_{\bar{h}}, \overline{\kappa}_{\bar{h}}, \alpha_{\bar{h}}, \mathbf{u}_{\bar{h}}, \bar{h})$ (where $\bar{h}$ can be computed by averaging the fluctuation displacement) and then can recover $(\overline{S}_0, \overline{\kappa}_0, \overline{\alpha}_0, \mathbf{u}_0, 0)$ using the relationships above, combined with $\mathbf{u}_0 = \overline{S}_0 \overline{S}_{\bar{h}}^{-1}(\mathbf{u}_{\bar{h}} - \bar{h}\mathbf{e}^3)$. This fluctuation displacement transformation formula follows from the entire linear-plus-periodic deformation $S_{\bar{h}}\mathbf{X} + \mathbf{u}_{\bar{h}}$ needing to stretch by $S_0(S_{\bar{h}})^{-1}$ into $S_0\mathbf{X} + S_0(S_{\bar{h}})^{-1}\mathbf{u}_{\bar{h}}$ in addition to vertically translating. Because all states in the equivalence class share the same energy, a vertical pin constraint on any one vertex simply picks one of the states and does no work.

Similar conversions must be applied to the equilibrium derivatives used to calculate stiffness, transforming them to maintain a vertically centered midsurface ($\dot{\bar{h}} = 0$). We note the following derivative relationships:

$$\dot{\overline{\kappa}}_0 = -\frac{1}{(\bar{h} + 1/\overline{\kappa}_{\bar{h}})^2}\left(\dot{\bar{h}} - \frac{\dot{\overline{\kappa}}_{\bar{h}}}{\overline{\kappa}_{\bar{h}}^2}\right) = \left(\frac{\overline{\kappa}_0}{\overline{\kappa}_{\bar{h}}}\right)^2\left(\dot{\overline{\kappa}}_{\bar{h}} - \overline{\kappa}_{\bar{h}}^2\dot{\bar{h}}\right),$$

$$\dot{\overline{S}}_0 = (\dot{\bar{h}}\overline{\kappa}_{\bar{h}}\hat{\mathbf{a}}^\perp \otimes \hat{\mathbf{a}}^\perp + \bar{h}\dot{\overline{\kappa}}_{\bar{h}}\hat{\mathbf{a}}^\perp \otimes \hat{\mathbf{a}}^\perp)\overline{S}_{\bar{h}} + (I + \bar{h}\overline{\kappa}_{\bar{h}}\hat{\mathbf{a}}^\perp \otimes \hat{\mathbf{a}}^\perp)\dot{\overline{S}}_{\bar{h}},$$

$$\dot{\mathbf{u}}_0 = \left(\dot{\overline{S}}_0 \overline{S}_{\bar{h}}^{-1} - \overline{S}_0 \overline{S}_{\bar{h}}^{-1}\dot{\overline{S}}_{\bar{h}}\overline{S}_{\bar{h}}^{-1}\right)(\mathbf{u}_{\bar{h}} - \bar{h}\mathbf{e}^3) + \overline{S}_0 \overline{S}_{\bar{h}}^{-1}(\dot{\mathbf{u}}_{\bar{h}} - \dot{\bar{h}}\mathbf{e}^3).$$

If we apply these formulas around an equilibrium state *that has already been transformed to have* $\bar{h} = 0$, then they simplify to:

$$\dot{\overline{\kappa}}_0 = \dot{\overline{\kappa}}_{\bar{h}} - \overline{\kappa}_0^2\dot{\bar{h}},$$

$$\dot{\overline{S}}_0 = (\dot{\bar{h}}\overline{\kappa}_{\bar{h}}\hat{\mathbf{a}}^\perp \otimes \hat{\mathbf{a}}^\perp)\overline{S}_0 + \dot{\overline{S}}_{\bar{h}},$$

$$\dot{\mathbf{u}}_0 = \left(\dot{\overline{S}}_0 \overline{S}_0^{-1} - \dot{\overline{S}}_{\bar{h}}\overline{S}_0^{-1}\right)\mathbf{u}_0 + (\dot{\mathbf{u}}_{\bar{h}} - \dot{\bar{h}}\mathbf{e}^3).$$

Finally, when computing stiffness around an unbent equilibrium state ($\overline{\kappa}_0 = 0$), these formulas simplify to:

$$\dot{\overline{\kappa}}_0 = \dot{\overline{\kappa}}_{\bar{h}},$$

$$\dot{\overline{S}}_0 = \dot{\overline{S}}_{\bar{h}},$$

$$\dot{\mathbf{u}}_0 = \dot{\mathbf{u}}_{\bar{h}} - \dot{\bar{h}}\mathbf{e}^3.$$

Therefore, after computing the equilibrium state perturbation $(\dot{\overline{S}}_{\bar{h}}, \dot{\overline{\kappa}}_{\bar{h}}, \overline{\alpha}, \dot{\mathbf{u}}_{\bar{h}}, \dot{\bar{h}})$ for scalar "independent" variable perturbation $\dot{\bar{y}} = 1$ via sensitivity analysis employing any strategy for constraining vertical motion, we can use the above formulas to transform to an equivalent perturbation $(\dot{\overline{S}}_0, \dot{\overline{\kappa}}_0, \overline{\alpha}, \dot{\mathbf{u}}_0, 0)$ and finally normalize this entire result so that $\dot{\bar{y}} = 1$.

# 4 Periodic Volume Calculation

We prove here the fact used in the main paper that the integrated normal vector of a surface depends only on the surface's boundary.

$$
\begin{aligned}
\int_{\Gamma_i^+} \mathbf{n}\, dA(\mathbf{x}) &= \sum_i \mathbf{e}_i \left( \int_{\Gamma_i^+} \mathbf{n} \cdot \mathbf{e}_i\, dA(\mathbf{x}) \right) \\
&= \frac{1}{2} \sum_i \mathbf{e}_i \left( \int_{\Gamma_i^+} \mathbf{n} \cdot \nabla \times (\mathbf{e}_i \times \mathbf{x})\, dA(\mathbf{x}) \right) \\
\text{(Stokes' Theorem)} \quad &= \frac{1}{2} \sum_i \mathbf{e}_i \left( \int_{\partial \Gamma_i^+} (\mathbf{e}_i \times \mathbf{x}) \cdot d\mathbf{s} \right) \\
&= \frac{1}{2} \sum_i \mathbf{e}_i \left( \mathbf{e}_i \cdot \int_{\partial \Gamma_i^+} \mathbf{x} \times d\mathbf{s} \right) = \frac{1}{2} \int_{\partial \Gamma_i^+} \mathbf{x} \times d\mathbf{s},
\end{aligned}
$$

where we used the identity $\nabla \times (\mathbf{e}_i \times \mathbf{x}) = \mathbf{e}_i \nabla \cdot \mathbf{x} - (\nabla \mathbf{x})\mathbf{e}_i = 2\mathbf{e}_i$ to rewrite $\mathbf{e}_i$ as a curl in the first step.

# 5 Analytical Bending Regularization Coefficients

We obtain analytical expressions for the inner integral appearing in our bending regularization:

$$
E_{\text{bend}}(f, \mathbf{p}) := \int_{\mathcal{M}} \int_0^{2\pi} \kappa_{\mathcal{M}}(\alpha)^2 k_b(\alpha; \mathbf{p}) d\alpha\, dA(\mathbf{x}).
$$

We first plug in our expansion for bending stiffness $k_b(\alpha; \mathbf{p})$ along with Euler's theorem for normal curvature, $\kappa_{\mathcal{M}}(\alpha) = \kappa_1 \cos^2(\alpha + \delta) + \kappa_2 \sin^2(\alpha + \delta)$:

$$
E_{\text{bend}}(f, \mathbf{p}) = \int_{\mathcal{M}} \int_0^{2\pi} (\kappa_1 \cos^2(\alpha + \delta) + \kappa_2 \sin^2(\alpha + \delta))^2 \left( \sum_{i=0}^4 q_i(\mathbf{p}) \cos(\overline{\alpha})^{4-i} \sin(\overline{\alpha})^i \right) d\alpha\, dA(\mathbf{x}).
$$

Here, phase offset $\delta$ accounts for the angle between the principal curvature directions of the target surface and the coordinate frame of the pattern parameter. The inner integral can be computed analytically to obtain:

$$
E_{\text{bend}}(f, \mathbf{p}) = \int_{\mathcal{M}} \left( \sum_{i=0}^4 q_i(\mathbf{p}) g_i(\delta, \kappa_1, \kappa_2) \right) dA(\mathbf{x}),
$$

with

$$
\begin{aligned}
\mathbf{g}(\delta, \kappa_1, \kappa_2) = \frac{1}{64}\pi \Big[ &-2\kappa_1\kappa_2(\cos(4\delta) - 6) + 16\left(\kappa_1^2 - \kappa_2^2\right)\cos(2\delta) + \left(\kappa_1^2 + \kappa_2^2\right)(\cos(4\delta) + 18), \\
&2\left(\kappa_1 - \kappa_2\right)\sin(2\delta)\left((\kappa_2 - \kappa_1)\cos(2\delta) - 4\left(\kappa_1 + \kappa_2\right)\right), \\
&\kappa_1\kappa_2(\cos(4\delta) + 2) - \left(\kappa_1^2 + \kappa_2^2\right)(\cos(4\delta) - 6), \\
&2\left(\kappa_1 - \kappa_2\right)\sin(2\delta)\left((\kappa_1 - \kappa_2)\cos(2\delta) - 4\left(\kappa_1 + \kappa_2\right)\right), \\
&-2\kappa_1\kappa_2(\cos(4\delta) - 6) + 16\left(\kappa_2^2 - \kappa_1^2\right)\cos(2\delta) + \left(\kappa_1^2 + \kappa_2^2\right)(\cos(4\delta) + 18) \Big].
\end{aligned}
$$

# 6 Homogenization statistics for the three pattern families

The following table summarizes the parameters and a few statistics from our homogenization experiments for the three pattern families used for inverse design in our work. For the parameters range, $s$ is the side length of the unit cell.

| Pattern Family | Parameters | Sampling Grid Dimensions | Parameters range | Data Generation Duration(s) |
|---|---|---|---|---|
| Cosine curve | amplitude | 50 | $[0, 0.5s]$ | 1042.36 |
| Dash line | length, orientation | $21 \times 16$ | $[0.2s, s] \times [\pi/4, \pi/2]$ | 3417.28 |
| Elliptic holes | orientation, lengths of the major and semi-major axes | $16 \times 9 \times 6$ | $[0, \pi/4] \times [0.04s, 0.36s] \times [0.52s, 0.72s]$ | 4540.10 |

# 7 Coarsened Design Optimization Weight Tuning

The objective function for the coarsened design optimization contains the fitting term, bending term, and the regularizaiton term which has pattern orientation smoothing and pattern parameters smoothing. In practice, we find it helpful to schedule the weights for these terms to gradually enforce one objective at a time. In the following, we provide the weight tuning schemes used for all the results in the main paper:

1. Starting from the output of the local-global optimization, run the design optimization with only the fitting objective and the flattening $f$ fixed for 600 iterations.

2. Free $f$, add the pattern orientation smoothing term with a weight such that the weighted value of the gradient norm of the pattern orientation term is 4 times the gradient norm of the fitting term. Run for 200 iterations.

3. Add the pattern parameter smoothing term with a weight such that the weighted value of the gradient norm of the pattern parameter term is 4 times the gradient norm of the fitting term. Run for 100 iterations. Reduce the orientation smoothing weight by half, run for another 100 iterations.

4. Add the bending term with a weight such that the weighted value of the gradient norm of the bending term is 2 times the gradient norm of the fitting term. Run for 400 iterations. Reduce the pattern parameter smoothing weight by half, reduce the pattern orientation smoothing weight by a quarter, run for another 200 iterations. Further reduce the pattern orientation smoothing weight by half, run for another 200 iterations.

# References

[Panetta et al., 2021] Panetta, J., Isvoranu, F., Chen, T., Siéfert, E., Roman, B., and Pauly, M. (2021). Computational inverse design of surface-based inflatables. *ACM Transactions on Graphics (TOG)*, 40(4):1–14.

[Ren et al., 2024] Ren, Y., Panetta, J., Suzuki, S., Kusupati, U., Isvoranu, F., and Pauly, M. (2024). Computational homogenization for inverse design of surface-based inflatables. *ACM Transactions on Graphics (TOG)*, 43(4):1–18.

[Sperl et al., 2020] Sperl, G., Narain, R., and Wojtan, C. (2020). Homogenized yarn-level cloth. *ACM Transactions on Graphics (TOG)*, 39:48:1 – 48:15.